
INTRUSIVE AND NON-INTRUSIVE MODEL ORDER REDUCTION FOR AIRBORNE CONTAMINANT TRANSPORT: COMPARATIVE ANALYSIS AND UNCERTAINTY QUANTIFICATION

PREPRINT ISSUED BY THE INSTITUTE FOR THE PROTECTION OF TERRESTRIAL INFRASTRUCTURES,
GERMAN AEROSPACE CENTER (DLR)

✉ **Lisa Kühn**^{*1}, ✉ **Jacopo Bonari**¹, ✉ **Max v. Danwitz**¹, and ✉ **Alexander Popp**^{1,2}

¹German Aerospace Center (DLR), Institute for the Protection of Terrestrial Infrastructures, Rathausallee 12, 53757 St. Augustin, Germany

²University of the Bundeswehr Munich, Institute for Mathematics and Computer-Based Simulation, Werner-Heisenberg-Weg 39, 85577 Neubiberg, Germany

February 26, 2026

ABSTRACT

Numerical simulations of contaminant dispersion, as after a gas leakage incident on a chemical plant, can provide valuable insights for both emergency response and preparedness. Simulation approaches combine incompressible Navier-Stokes (INS) equations with advection-diffusion (AD) processes to model wind and concentration field. However, the computational cost of such high-fidelity simulations increases rapidly for complex geometries like urban environments, making them unfeasible in time-critical or multi-query "what-if" scenarios. Therefore, this study focuses on the application of model order reduction (MOR) techniques enabling fast yet accurate predictions. To this end, a thorough comparison of intrusive and non-intrusive MOR methods is performed for the computationally more demanding parametric INS problem with varying wind velocities. Based on these insights, a non-intrusive reduced-order model (ROM) is constructed accounting for both wind velocity and direction. The study is conducted on a two-dimensional domain derived from real-world building footprints, preserving key features for analyzing the dispersion of, for instance, denser contaminants. The resulting ROM enables faster than real-time predictions of spatio-temporal contaminant dispersion from an instantaneous source under varying wind conditions. This capability allows assessing wind measurement uncertainties through a Monte Carlo analysis. To demonstrate the practical applicability, an interactive dashboard provides intuitive access to simulation results.

Keywords Reduced-order modeling · Airborne contaminant transport · Urban physics · Intrusive and non-intrusive MOR · Proper orthogonal decomposition

1 Introduction

So-called CBRN events, i.e., chemical, biological, radiological and nuclear events, caused either by accident, sabotage or terrorism pose high risks to persons and critical infrastructures. Among CBRN threats, a major role is played by chemical incidents and the subsequent atmospheric release of dangerous contaminants. In this context, the U.S. Chemical Safety Board alone reports more detailed investigations for 80 chemical incidents in the U.S. within the last five years [Owens et al., 2025], with hundreds of other incidents reported throughout the last decades around the world as analyzed in Bene et al. [2024], Gomez et al. [2008], Coming Clean Inc. [2023] and references therein. Computational modeling and simulation can help investigating the spatio-temporal contaminant dispersion in such cases. For this

*lisa.kuehn@dlr.de

purpose, tools such as *ADMS* [Carruthers et al., 1994], *ALOHA* [Jones et al., 2013] and *AERMOD* [Cimorelli et al., 2005] have been introduced estimating the contaminant concentration field based on a Gaussian plume model [Arystanbekova, 2004, Holzbecher, 2011, Snoun et al., 2023]. They assume a continuous point source for the contaminant and, based on given atmospheric conditions, calculate the downwind concentration under the assumption that the agent disperses according to a normal distribution in both horizontal and vertical directions. Although already successfully applied in different analysis scenarios as e.g. in Schneider et al. [2025], these estimates – in their basic form – do not include the influence of obstacles on the concentration field as it is expected in case the contaminant spreads across built-up areas. To overcome this and other limitations of plume models, more complex air dispersion models can be employed [Boris, 2002, Patnaik et al., 2012]. They can be broadly categorized in the three main families of Lagrangian, Eulerian and mixed models. An exhaustive, though unfortunately not up-to-date list of models employed in Europe can be found in Kukkonen et al. [2012]. Within the field of Eulerian computational fluid dynamics (CFD) models, the airborne contaminant transport can be modeled by employing steady-state incompressible Navier-Stokes (INS) equations to estimate the wind field and then solve a related advection diffusion (AD) problem, employing the computed wind field solution as advection field [Khamlich et al., 2023, von Danwitz et al., 2024, Ulfah et al., 2018]. Such models can offer a high accuracy and could theoretically be applied for predicting the contaminant transport in case of an incident or in preparation when studying different "what-if" case scenarios. Yet, their increased computational expense often prohibits the use for time-critical applications like chemical incidents and multi-query analysis, where the delivery of near real-time results is fundamental. To mitigate this problem, a promising solution is offered by the application of model order reduction (MOR) techniques, aiming for fast yet accurate results for the problem at hand. For this purpose, a reduced-order model (ROM) is derived that provides a good approximation of the full-order model (FOM), for example a high-fidelity CFD-based model, while it requires only a fraction of the computational resources compared to the FOM and can thereby be used instead of the FOM. For the considered application, the usage of MOR techniques is particularly well-suited, since the approximation of parametric partial differential equations is an active research area and major field of application of MOR methods [Roza et al., 2022, Quarteroni et al., 2015, Benner et al., 2021, 2020].

To enable fast evaluation times of the ROM, a strict online-offline decomposition has to be employed. This includes an offline phase where snapshot solutions of the FOM are taken for several parameter value samples. Based on these, the ROM is set up such that evaluations during the online phase are completely independent of the FOM and can hence be performed in very little time. Generally, such reduction methods can be distinguished into two types: intrusive and non-intrusive methods. Intrusive methods like the proper orthogonal decomposition (POD) with a subsequent Galerkin projection of the FOM operators (PODG) [Quarteroni et al., 2015, Pichi et al., 2022, Quarteroni, 2014, Hesthaven et al., 2016] are based on the physics-based model formulation and their implementation requires intruding the respective numerical solver, that can be, e.g., a finite element formulation. Non-intrusive methods like POD with interpolation (PODI) [Tezzele et al., 2022, Yu et al., 2019, Czech et al., 2022], on the other hand, only rely on the high-fidelity data – coming either from (FOM) simulations or directly from measurements – and use data-fitted meta-models or machine learning when setting up the ROM [Czech et al., 2022]. Whereas intrusive methods are based on the physical relationships and therefore often provide reliable and physically meaningful results [Conti et al., 2024], and can even provide reasonable results slightly outside the trained parameter range [Czech et al., 2022], they often come with a lower speed-up [Czech et al., 2022], high expenses for potential hyper-reduction steps [Ballarin et al., 2015a], and a limited flexibility in terms of full-order simulators [Conti et al., 2024]. Non-intrusive ROMs on the other hand can also be applied in case of a closed-source numerical solver for the FOM as it is the case for commercial solvers. On the downside, these methods are known to need a lot of training data for approximating the FOM behavior, leading to a heavy offline phase [Yu et al., 2019, Czech et al., 2022, Vinuesa and Brunton, 2022]. Depending on the method used for interpolation or regression, a potential vulnerability to overfitting and sensitive hyper-parameters can be observed [Czech et al., 2022]. Specific additional challenges of especially deep-learning approaches within this class of MOR methods are their interpretability as well as the enforcement of physical knowledge and sparsity on the ROM [Vinuesa and Brunton, 2022]. One drawback of both PODI and PODG is the linear subspace that is spanned by POD-based approaches, making it difficult to adequately represent problems featuring a slowly decaying Kolmogorov n -width [Regazzoni et al., 2024]; that means, problems that are not well suited for an approximation on a small n -dimensional linear subspace as created by POD. Thus, a large reduced basis (RB) is needed for, e.g., high Reynolds numbers in flow problems to gain a good approximation quality of the FOM [Pichi et al., 2022, Regazzoni et al., 2024]. Although the INS problem considered in this study is indeed nonlinear, linear methods are widely applied to it and can be observed to still provide a sufficiently good approximation [Khamlich et al., 2023, Veiga-Piñeiro et al., 2025].

Contaminant dispersion simulations with and without ROMs can be found for many applications such as air pollution research [Khamlich et al., 2023, Masoumi-Verki et al., 2022, Arcucci et al., 2023], wild fire research [Reisch et al., 2024, Zhong et al., 2023] or health sciences [Schuster et al., 2025]. Furthermore, research on computational fluid mechanics in the context of unmanned aerial vehicles can be found, e.g., in Veiga-Piñeiro et al. [2025], Chinesta et al. [2025] considering different inflow wind velocities and directions. The latter is also the case in Khamlich et al. [2023], where a

hybrid ROM is introduced for the INS and AD problem consisting of an intrusive PODG scheme in combination with hyper-reduction for the AD problem and non-intrusive POD with interpolation for the Reynolds-averaged Navier-Stokes equations. For the case considered here, i.e., gas leakage in the context of a chemical accident, the authors in Ritter et al. [2016], Mattuschka et al. [2025] present a MOR approach for the advection-diffusion problem, considering a constant wind field. Although these publications provide impressive results, to the best of the authors' knowledge they always use either intrusive or non-intrusive methods. However, thorough comparisons, while highly relevant for transitioning into the real-life practice of critical infrastructure protection, have so far been extremely scarce and limited to academic examples or real-world structural mechanics [Padula et al., 2024, Czech et al., 2022] as well as to the rotating thermal shallow water equation in Karasözen et al. [2022]. Therefore, the aim and main contribution of this study is to offer the reader a comprehensive and quantitative comparison of the two approaches for the considered application under different wind velocities. Following the comparison of the popular intrusive PODG and the non-intrusive PODI, a reduced-order model is set up that is parametrized by wind velocity and direction. Since the study is mainly focused on a comparative analysis, a rather simple FOM is taken into account, featuring a laminar wind flow evaluated on a two-dimensional domain, intended as strategically valuable starting point. By simplifying the physics to a two-dimensional laminar flow governed by INS equations and the AD problem for the contaminant transport, the problem becomes tractable while preserving the core mathematical and physical structure of a full three-dimensional Eulerian model. This approach enables a systematic and effective evaluation of the accuracy and computational efficiency of the different MOR methods. The chosen approach therefore offers the benefits of (i) fostering the benchmarking process by enabling a clear comparison in terms of error, speed-up, data requirements and extrapolation capabilities; (ii) representing a first building block that can later be incrementally extended to include three-dimensional geometries and to include turbulence modeling via, e.g., Reynolds averaged Navier-Stokes (RANS) equations in future works; (iii) and finally guaranteeing the reduction of computational time when performing repeated high-fidelity simulations during the ROM development, significantly lowering computational costs and accelerating model development. It is also worth mentioning that the chosen computational domain is characterized by the presence of obstacles, rendered as realistic building footprints which are defined by the inclusion of real geo-referenced data from a public database as shown in Bonari et al. [2024]. On top of this, the developed model is thereafter evaluated within a probabilistic setting by performing a Monte Carlo analysis based on the developed ROM. The process accounts for modeled uncertainties within the inflow wind conditions, thus adding further value to the model outside the realm of a deterministic setting. Eventually, an interactive dashboard is presented as a first step towards an intuitive usage of simulation results as for example within a digital twin framework.

The remainder of the article is structured as follows: Section 2 reviews the mathematical and numerical modeling of the airborne contaminant transport problem as well as the considered MOR techniques. Subsequently, Section 3 provides a comparison between PODG and PODI for the flow problem at hand, parametrized for different inflow wind velocities. This is followed by an extension of the PODI-based ROM to also cover different wind directions. In Section 4, the presented MOR framework is applied to a crisis management scenario test-case, where modeled measurement uncertainties are considered within a Monte Carlo framework to analyze the sensitivity of the contaminant concentration field with respect to measurement inaccuracies. Here, the probabilistic nature of inflow wind measurements is taken into account. Finally, an interactive dashboard is shown, aiming at an easy accessibility and usability of the developed model. The article is concluded in Section 5, where possible future extensions of the study towards realistic three-dimensional turbulent flows are exposed.

2 Mathematical Formulation for Full- and Reduced-Order Model

2.1 Full-Order Model

The spreading of airborne contaminant within a two-dimensional bounded domain $\Omega \subseteq \mathbb{R}^2$ can be modeled by solving the steady-state incompressible Navier-Stokes equations first, and subsequently the advection diffusion problem. The INS equations for the wind velocity field \mathbf{u} and pressure value p reads as:

$$\begin{aligned}
 -\nu \nabla^2 \mathbf{u} + (\mathbf{u} \cdot \nabla) \mathbf{u} + \nabla p &= \mathbf{0} && \text{in } \Omega, \\
 \nabla \cdot \mathbf{u} &= 0 && \text{in } \Omega, \\
 \mathbf{u} &= \mathbf{g}_D(\boldsymbol{\mu}) && \text{on } \Gamma_D, \\
 \mathbf{u} &= \mathbf{0} && \text{on } \Gamma_0, \\
 \nu \frac{\partial \mathbf{u}}{\partial \mathbf{n}} - p \mathbf{n} &= \mathbf{0} && \text{on } \Gamma_N,
 \end{aligned} \tag{1}$$

where $\nu \in \mathbb{R}^+$ denotes the kinematic viscosity, Γ_0 no-slip boundaries at the buildings, and Γ_N the Neumann outflow boundary with \mathbf{n} being the outward-pointing normal to it. The effect of different inflow wind conditions is considered by the inhomogeneous Dirichlet boundary condition, which is parametrized by $\boldsymbol{\mu} \in \mathcal{D} \subset \mathbb{R}^d$, $d \in \{1, 2\}$, depending on whether only the inflow wind velocity or additionally the wind direction varies, too. Thus, also the velocity and pressure are parameter-dependent quantities $(\mathbf{u}, p) = (\mathbf{u}(\mathbf{x}, \boldsymbol{\mu}), p(\mathbf{x}, \boldsymbol{\mu}))$. The Reynolds number considered here accounts for the maximum velocity magnitude u_{\max} so that $\text{Re} = u_{\max} l/\nu$, where l is the characteristic length of the domain.

To enable a numerical solution for the wind field, the Navier-Stokes equations in Eq. (1) are converted from the strong form to the weak form and are then discretized using Taylor-Hood finite elements, as described in Ballarin et al. [2015a], Elman et al. [2014]. This leads to a discretized system of equations for the velocity at every finite element node and in each spatial direction $\mathbf{u}^h \in \mathbb{R}^{N_h}$ as well as the pressure value $\mathbf{p}^h \in \mathbb{R}^{N_{h,p}}$. Therein, N_h and $N_{h,p}$ represent the degrees of freedom related to the use of second-order Lagrange finite elements for the velocity and first-order Lagrange finite elements for the pressure. Following the derivations in [Ballarin et al., 2015a], the discretized form of the FOM can be written as:

$$\begin{bmatrix} \mathbf{A}(\boldsymbol{\mu}) + \mathbf{C}(\mathbf{u}(\boldsymbol{\mu}); \boldsymbol{\mu}) & \mathbf{B}^\top(\boldsymbol{\mu}) \\ \mathbf{B}(\boldsymbol{\mu}) & \mathbf{0} \end{bmatrix} \begin{bmatrix} \mathbf{u}^h(\boldsymbol{\mu}) \\ \mathbf{p}^h(\boldsymbol{\mu}) \end{bmatrix} = \begin{bmatrix} \mathbf{f}(\boldsymbol{\mu}) \\ \mathbf{g}(\boldsymbol{\mu}) \end{bmatrix} \quad (2)$$

with $\mathbf{A}, \mathbf{B}, \mathbf{C}, \mathbf{f}$ and \mathbf{g} containing the discretized terms of the problem [Ballarin et al., 2015a]. By means of the Newton-Raphson algorithm, implemented within the FEniCS framework [Alnaes et al., 2015], the emerging nonlinear system of equations is eventually solved for pressure and velocity. The implementation is validated for well-known benchmark problems shown in Elman et al. [2014].

Once the wind field has been computed by solving the INS equations, the spatio-temporal gas concentration $c(\mathbf{x}, t)$ is determined by solving of the following advection-diffusion problem

$$\begin{aligned} \frac{\partial c}{\partial t} - \kappa \nabla^2 c + \mathbf{u} \cdot \nabla c &= 0 && \text{in } \Omega \times (0, T), \\ \kappa \nabla c \cdot \mathbf{n} &= 0 && \text{in } (\Gamma_+ \cup \Gamma_0) \times (0, T), \\ c(\mathbf{x}, t) &= 0 && \text{in } \Gamma_- \times (0, T), \\ c(\mathbf{x}, 0) &= m(\mathbf{x}) && \text{in } \Omega, \end{aligned} \quad (3)$$

featuring the diffusion coefficient $\kappa \in \mathbb{R}^+$ as well as the wind field $\mathbf{u}(\mathbf{x}, \boldsymbol{\mu})$ calculated earlier. Following the definitions in [Elman et al., 2014], $\Gamma_+ \subset \partial\Omega$ denotes the outflow boundary with $\mathbf{u} \cdot \mathbf{n} > 0$, $\Gamma_0 \subset \partial\Omega$ the boundaries tangential to the flow such that $\mathbf{u} \cdot \mathbf{n} = 0$ and $\Gamma_- \subset \partial\Omega$ the inflow boundary with $\mathbf{u} \cdot \mathbf{n} < 0$. Selecting a first-order Lagrange finite element approach for the concentration and following [Brooks and Hughes, 1982, Behr, 2008, von Danwitz et al., 2023, Key et al., 2023], the SUPG-stabilized weak form for the boundary value problem can be derived. To address the time-dependent nature of the problem, an implicit backward Euler time-stepping algorithm is applied as described in Elman et al. [2014, Eq. (10.25)]. Altogether, space and time discretization ultimately lead to a linear system of equations to be solved for the unknown gas concentration field.

2.2 Reduced INS Problem

A ROM is constructed for the INS problem in Eq. (1) using two methods: the intrusive PODG approach combined with the discrete empirical interpolation method and the non-intrusive counterpart, POD with interpolation. In both approaches, a reduced basis is first generated by applying POD to the snapshot solutions obtained from the full-order model. The goal of both methods is to efficiently map unseen parameter values to their corresponding approximate solutions of Eq. (1).

Proper orthogonal decomposition

To construct a reduced basis via POD, snapshot solutions of the high-fidelity model are computed in a first step for specific training parameters $\boldsymbol{\mu}_s \in \Xi_s = \{\boldsymbol{\mu}_1, \dots, \boldsymbol{\mu}_{N_s}\}$, which are determined based on a-priori knowledge of the system. These N_s snapshots are collected as columns of the snapshot matrix $\mathbf{S} = [\mathbf{s}_1, \dots, \mathbf{s}_{N_s}]$, where $\mathbf{s}_i = \mathbf{s}(\boldsymbol{\mu}_i)$ is the FOM solution corresponding to the i^{th} parameter value in Ξ_s . For the specific application and the associated focus on the velocity, the following is shown for velocity snapshots, so that $\mathbf{s}_i = \mathbf{u}_i^h$ and $\mathbf{S} \in \mathbb{R}^{N_h \times N_s}$. However, similar relations hold for pressure snapshots, which would result in different dimensions than those presented here. Eventually, the aim of POD is to find a low-dimensional linear subspace $\mathcal{V} = \text{span}\{\mathbf{V}_1, \dots, \mathbf{V}_{N_{rb}}\}$, spanned by the column-orthogonal POD basis matrix $\mathbf{V} = [\mathbf{V}_1, \dots, \mathbf{V}_{N_{rb}}] \in \mathbb{R}^{N_h \times N_{rb}}$ such that the error

$$\delta_{\text{rb}} = \sum_{k=1}^{N_s} \|\mathbf{s}_k - \mathbf{V}\mathbf{V}^T\mathbf{s}_k\|_2^2 \quad (4)$$

between the snapshot matrix and its orthogonal projection onto \mathcal{V} is minimized [Benner et al., 2021]. Such a reduced basis can be found via a singular value decomposition (SVD) of the snapshot matrix

$$\mathbf{S} = \mathbf{U}\mathbf{\Sigma}\mathbf{Z}^T, \quad (5)$$

with $\mathbf{U} = [\Phi_1, \dots, \Phi_{N_h}] \in \mathbb{R}^{N_h \times N_h}$ as well as $\mathbf{Z} = [\Psi_1, \dots, \Psi_{N_s}] \in \mathbb{R}^{N_s \times N_s}$ being orthogonal matrices, and $\mathbf{\Sigma} = \text{diag}(\sigma_1, \dots, \sigma_r) \in \mathbb{R}^{N_h \times N_s}$ the eigenvalue matrix where $r \leq \min(N_h, N_s)$ denotes the rank of the snapshot matrix and $\sigma_1 \geq \sigma_2 \geq \dots \geq \sigma_r$ [Quarteroni et al., 2015]. From the SVD, it follows that

$$\mathbf{S}\Psi_i = \sigma_i\Phi_i \quad \text{and} \quad \mathbf{S}^T\Phi_i = \sigma_i\Psi_i, \quad i = 1, \dots, r. \quad (6)$$

Inserting the two expressions into each other leads to the equivalent formulation

$$\mathbf{S}^T\mathbf{S}\Psi_i = \sigma_i^2\Psi_i \quad \text{and} \quad \mathbf{S}\mathbf{S}^T\Phi_i = \sigma_i^2\Phi_i, \quad i = 1, \dots, r. \quad (7)$$

The eigenvalue problems in Eq. (7) enable an efficient determination of the basis functions without having to solve the full singular value decomposition. Furthermore, since the number of degrees of freedom commonly vastly exceeds the number of snapshots, it is computationally more preferable to solve the first eigenvalue problem in Eq. (7) featuring the symmetric positive-definite correlation matrix $\mathbf{C} = \mathbf{S}^T\mathbf{S} \in \mathbb{R}^{N_s \times N_s}$, or $C_{ij} = (s_i, s_j)_{L^2}$, respectively [Quarteroni et al., 2015, Benner et al., 2020, Khamlich et al., 2023]. Although beneficial in terms of computational resources, the authors in [Ballarin et al., 2015a] warn that constructing the reduced basis via the correlation matrix may lead to poorer conditioning. Eventually, the desired basis functions Φ_i can be gained by means of the eigenvectors of the correlation matrix Ψ_i by reformulating the relation in Eq. (6) as

$$\Phi_i = \frac{1}{\sigma_i} \mathbf{S}\Psi_i, \quad i = 1, \dots, N_{\text{rb}}. \quad (8)$$

In the following, a truncation is performed to retain only information associated with the largest $N_{\text{rb}} \ll N_h$ eigenvalues of the corresponding eigenvectors of $\mathbf{S}\mathbf{S}^T$, along their corresponding eigenvectors. These eigenvectors span the desired reduced subspace \mathcal{V} , and are used to construct the basis matrix $\mathbf{V} = [\Phi_1, \dots, \Phi_{N_{\text{rb}}}] \in \mathbb{R}^{N_h \times N_{\text{rb}}}$ [Benner et al., 2021]. Repeating the procedure for the pressure, a subspace \mathcal{P} is found that is spanned by the columns of $\mathbf{P} = [\Upsilon_1, \dots, \Upsilon_{N_{\text{rb},p}}] \in \mathbb{R}^{N_h \times N_{\text{rb},p}}$. With the parameter-independent eigenvectors – also called POD modes – quantities can eventually be approximated by a linear combination of POD modes as well as parameter-dependent coefficients

$$\mathbf{u}^h(\boldsymbol{\mu}) \approx \sum_{i=1}^{N_{\text{rb}}} a_i(\boldsymbol{\mu})\Phi_i = \mathbf{V}\mathbf{a}(\boldsymbol{\mu}) \quad \text{and} \quad \mathbf{p}^h(\boldsymbol{\mu}) \approx \sum_{i=1}^{N_{\text{rb},p}} b_i(\boldsymbol{\mu})\Upsilon_i = \mathbf{P}\mathbf{b}(\boldsymbol{\mu}). \quad (9)$$

While the first formulation of the approximation above emphasizes the POD modes and coefficients, it is often equivalently expressed as a matrix vector multiplication of the basis matrices \mathbf{V} and \mathbf{P} , and the POD coefficients $\mathbf{a}(\boldsymbol{\mu}) \in \mathbb{R}^{N_{\text{rb}}}$ and $\mathbf{b}(\boldsymbol{\mu}) \in \mathbb{R}^{N_{\text{rb},p}}$. The latter are hereby referred to as the reduced velocity $\hat{\mathbf{u}}(\boldsymbol{\mu}) \in \mathbb{R}^{N_{\text{rb}}}$ and pressure $\hat{\mathbf{p}}(\boldsymbol{\mu}) \in \mathbb{R}^{N_{\text{rb},p}}$, i.e., $\hat{\mathbf{u}}(\boldsymbol{\mu}) = \mathbf{a}(\boldsymbol{\mu})$ and $\hat{\mathbf{p}}(\boldsymbol{\mu}) = \mathbf{b}(\boldsymbol{\mu})$.

Due to the fact that the error introduced by POD is directly proportional to the magnitude of the neglected eigenvalues [Benner et al., 2020], a fast decay of the eigenvalues is crucial for a good approximation quality. A measure of the retained energy can be given as

$$E_{\text{rb}} = \frac{\sum_{i=1}^{N_{\text{rb}}} \sigma_i}{\sum_{k=1}^r \sigma_k} \in [0, 1]. \quad (10)$$

Therefore, slowly decaying eigenvalues, and with that a slowly decaying Kolmogorov n-width, indicate that the system at hand is not easily reducible by introducing a low-dimensional subspace as derived here. Once the reduced basis is established, the full-order solutions for any given parameter value can be approximated by solving either a projected system of equations (PODG) or an interpolation/regression task (PODI) to determine the POD coefficients, i.e., the reduced velocity and pressure.

POD with Galerkin projection

As described in the previous paragraph, PODG utilizes the computed reduced basis functions, also known as the POD modes, for velocity and pressure, to project the system of equations of the FOM onto the subspaces they span. By further replacing the full-order quantities with the approximation as shown in Eq. (9), the system of equations to be

solved online reduces to the size of the reduced basis for velocity and pressure. By performing a Galerkin projection on the discretized system of equations in Eq. (2), the residual that results from replacing \mathbf{u}^h with the approximation in Eq. (9) is orthogonal to the subspace spanned by the columns of \mathbf{V} and \mathbf{P} , i.e., the POD modes [Ballarin et al., 2015a]. This can be written as

$$\begin{aligned} \mathcal{R} &= \begin{bmatrix} \mathbf{A}(\boldsymbol{\mu}) + \mathbf{C}(\mathbf{V}\hat{\mathbf{u}}(\boldsymbol{\mu}); \boldsymbol{\mu}) & \mathbf{B}^\top(\boldsymbol{\mu}) \\ \mathbf{B}(\boldsymbol{\mu}) & \mathbf{0} \end{bmatrix} \begin{bmatrix} \mathbf{V}\hat{\mathbf{u}}(\boldsymbol{\mu}) \\ \mathbf{P}\hat{\mathbf{p}}(\boldsymbol{\mu}) \end{bmatrix} - \begin{bmatrix} \mathbf{f}(\boldsymbol{\mu}) \\ \mathbf{g}(\boldsymbol{\mu}) \end{bmatrix} \\ &\Rightarrow \begin{bmatrix} \mathbf{V}^\top & \mathbf{0} \\ \mathbf{0} & \mathbf{P}^\top \end{bmatrix} \mathcal{R} = \mathbf{0}. \end{aligned} \quad (11)$$

With that, the reduced set of equations can be expressed as [Ballarin et al., 2015a]:

$$\begin{bmatrix} \hat{\mathbf{A}}(\boldsymbol{\mu}) + \hat{\mathbf{C}}(\hat{\mathbf{u}}(\boldsymbol{\mu}); \boldsymbol{\mu}) & \hat{\mathbf{B}}^\top(\boldsymbol{\mu}) \\ \hat{\mathbf{B}}(\boldsymbol{\mu}) & \mathbf{0} \end{bmatrix} \begin{bmatrix} \hat{\mathbf{u}}(\boldsymbol{\mu}) \\ \hat{\mathbf{p}}(\boldsymbol{\mu}) \end{bmatrix} = \begin{bmatrix} \hat{\mathbf{f}}(\boldsymbol{\mu}) \\ \hat{\mathbf{g}}(\boldsymbol{\mu}) \end{bmatrix} \quad (12)$$

with

$$\begin{aligned} \hat{\mathbf{A}} &= \mathbf{V}^\top \mathbf{A} \mathbf{V}, \quad \hat{\mathbf{C}} = \mathbf{V}^\top \mathbf{C} \mathbf{V}, \quad \hat{\mathbf{f}} = \mathbf{V}^\top \mathbf{f}, \\ \hat{\mathbf{B}} &= \mathbf{P}^\top \mathbf{B} \mathbf{P}, \quad \hat{\mathbf{g}} = \mathbf{V}^\top \mathbf{g}. \end{aligned}$$

Although this description is based on formulating the projection as matrix multiplication to the discretized operators stemming from the weak form of Eq. (1), other ways of formulating it can be found in literature, which rely on the superposition of POD modes scaled by their coefficients as shown in [Khamlich et al., 2023, Hijazi et al., 2023, Lorenzi et al., 2016]. However, the result is eventually the same – a nonlinear system of equations for the POD coefficients of Eq. (9) for any new parameter value. Since the implementation of the steps above require access to the solver, the PODG approach is an intrusive approach.

To enable an efficient online-offline decomposition, parameter-dependent terms in the equations above are affinely decomposed into a parameter-dependent factor and a parameter-independent matrix or vector [Ballarin et al., 2015a, Sec. 2.3]. However, an approximation of the affine decomposition has to be introduced for the convective term due to its nonlinearity. Therefore, the discrete empirical interpolation method (DEIM) [Chaturantabud and Sorensen, 2010] is applied here. Since a detailed description of DEIM is beyond the scope of this article, interested readers can find further information in Quarteroni et al. [2015], Khamlich et al. [2023], Rozza et al. [2024].

POD with interpolation

Although the initial steps of PODI [Bui-Thanh et al., 2003] – computing snapshots and constructing a reduced basis via POD – are identical to those in PODG, PODI operates non-intrusively by using interpolation or regression methods instead of a Galerkin projection for mapping unknown input parameter values to POD coefficients. For this purpose, PODI relies solely on the snapshot data. Hence, rather than projecting the system of equations, only the snapshot data is projected:

$$\mathbf{S} \approx \mathbf{V}\hat{\mathbf{S}} \quad \text{or} \quad \mathbf{s}(\boldsymbol{\mu}_k) \approx \sum_{i=1}^{N_{\text{rb}}} \hat{s}_i(\boldsymbol{\mu}_k) \boldsymbol{\Phi}_i \quad (13)$$

with $\hat{\mathbf{S}} = \mathbf{V}^\top \mathbf{S}$ or $\hat{s}_i(\boldsymbol{\mu}_k) = (\boldsymbol{\Phi}_i, \mathbf{s}(\boldsymbol{\mu}_k))_{L^2}$ and $k = 1, \dots, N_s$, respectively. Here, $\hat{\mathbf{S}} \in \mathbb{R}^{N_{\text{rb}} \times N_s}$ and $\hat{s}_i(\boldsymbol{\mu}_k) \in \mathbb{R}$ denote the POD coefficients in Eq. (9) for an approximation of the FOM solutions collected inside the snapshot matrix. This set of known POD coefficients is now used to set up an approximation of the mapping between parameter values and POD coefficients $\mathbf{f} : \mathcal{D} \rightarrow \mathbb{R}^{N_{\text{rb}}}$, $\boldsymbol{\mu} \mapsto \mathbf{a}$ by means of an interpolation or regression scheme $\boldsymbol{\pi} : \mathcal{D} \rightarrow \mathbb{R}^{N_{\text{rb}}}$. To enable such a mapping, the set of training parameter values Ξ_s is needed as isolated input and therefore has to be stored separately with the i^{th} parameter value corresponding to the i^{th} snapshot. The interpolation or regression can then be performed with various algorithms such as radial basis function (RBF) interpolation, Gaussian process regression or artificial neural networks [Yu et al., 2019, Bērziņš et al., 2020]. For the RBF interpolation as used here, $\boldsymbol{\pi}(\boldsymbol{\mu})$ reads as:

$$\boldsymbol{\pi}(\boldsymbol{\mu}) = \sum_{k=1}^{N_s} \mathbf{w}_k \varphi(\|\boldsymbol{\mu} - \boldsymbol{\mu}_k\|), \quad \text{where} \quad \pi_i(\boldsymbol{\mu}_k) = \hat{s}_i(\boldsymbol{\mu}_k), \quad i = 1, \dots, N_{\text{rb}}. \quad (14)$$

Here, the scalar-valued radial basis function $\varphi(d)$ corresponds to the Euclidean distance d between a chosen sample point $\boldsymbol{\mu}$ and a so-called center, in this case the parameter values $\boldsymbol{\mu}_k$ that were considered when taking the snapshots. There exist many different radial basis functions in literature, and one example – which is employed going forward – is the thin-plate spline $\varphi(d) = d^2 \log(d)$. Additionally, $\mathbf{w}_k \in \mathbb{R}^{N_{\text{rb}}}$ denotes the k^{th} weighting vector that is set up offline

such that the POD coefficients $\hat{s}_i(\boldsymbol{\mu}_k)$ stemming from the snapshots can be reproduced exactly [Bērziņš et al., 2020, Xiao et al., 2015].

Following the offline phase consisting of the projection of snapshot data and computing the weighting vectors, Eq. (14) can be evaluated for new parameter values, delivering interpolated POD coefficients to eventually approximate the FOM solution. Thus, the approximation in Eq. (9) can be written as

$$\mathbf{u}^h(\boldsymbol{\mu}) \approx \sum_{i=1}^{N_{\text{rb}}} \pi_i(\boldsymbol{\mu}) \boldsymbol{\Phi}_i = \mathbf{V}\boldsymbol{\pi}(\boldsymbol{\mu}), \quad (15)$$

where POD coefficients are approximated by the interpolation scheme for any new parameter value $\boldsymbol{\mu}$, so that $a_i(\boldsymbol{\mu}) \approx \pi_i(\boldsymbol{\mu})$.

3 Numerical Examples

3.1 Comparing PODG and PODI for INS with varying inflow wind velocities

Due to the downstream relevance in the discussed applications (Sec. 4) we focus on evaluating of the ROM for the wind field and omit the discussion of the pressure field results. To compare the performance of PODG with its non-intrusive counterpart PODI, the wind field is reduced for two different real-world geometries of varying complexity, referred to as Geometry 1 and Geometry 2. The computational domains are derived as shown in [Bonari et al., 2024], and their mesh discretization can be seen in Fig. 1. The setup follows Sec. 2.1, with additional details provided in Table 1. Due to the constant wind direction, the characteristic length used in the Reynolds number is chosen to be the inflow boundary.

To assess the reducibility of the problem, the normalized eigenvalues $\sigma_i/\sigma_{\text{max}}$ of the correlation matrix are analyzed and the results are shown in Fig. 2a. It can be observed, that for both geometries, the respective eigenvalues decay quickly, indicating that both problems are well-suited for finding an appropriate approximation within a low-dimensional subspace. In Fig. 2b, the retained energy is also shown as a first indicator of the necessary size of the reduced basis. To ensure a fair comparison of the two reduction methods, identical sets of snapshot data are used for both methods in terms of training and testing.

PODG

Since the INS problem is nonlinear, the PODG approach is combined with the discrete empirical interpolation method [Chaturantabut and Sorensen, 2010] for the convective term as described in the previous section. The respective parameters for the ROM can be found in Table 2. Note that training and testing parameter values are sampled equidistantly throughout the parameter space. The implementation used in this study is based on the open-source tool *RBniCS* [Ballarin et al., 2015b, Rozza et al., 2024].

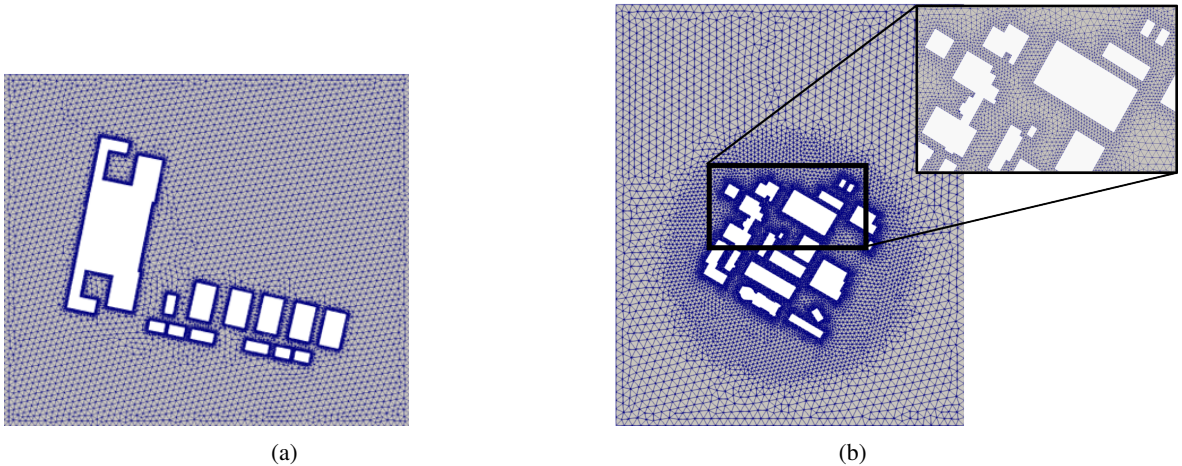


Figure 1: Meshed computational domains. Geometry 1 (a) features a sparse set of buildings, while Geometry 2 (b) represents a denser development. Both domains are based on buildings footprints derived from real, geo-referenced data, cf. [Bonari et al., 2024].

Table 1: Parameters of the full-order models considered for the comparison between PODG and PODI.

Parameter	Numerical Examples	
	Geometry 1	Geometry 2
Degrees of freedom	64,122	71,742
Reynolds number	$\text{Re} \in [5.5, 205]$	$\text{Re} \in [10, 380]$
Inflow wind velocity m s^{-1}	$w_i \in [0.5, 20]$	$w_i \in [0.5, 20]$
Inflow wind direction	South	South

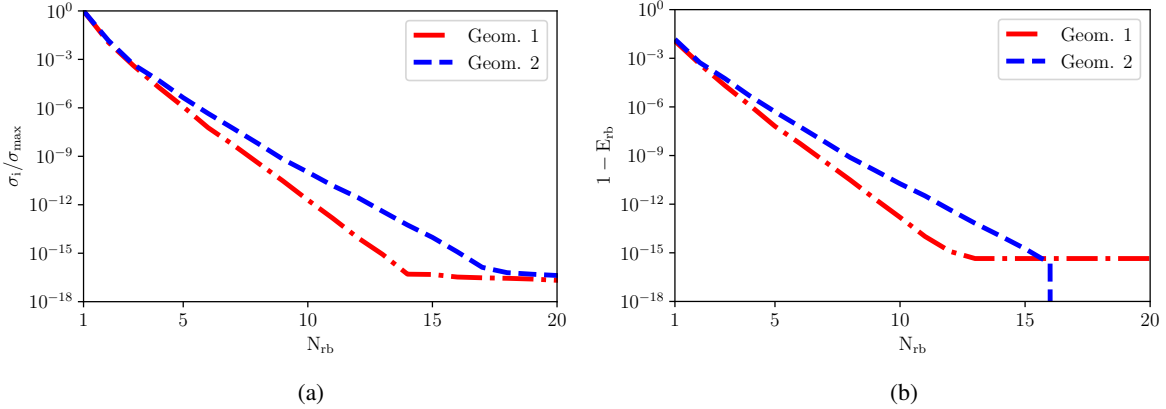


Figure 2: Normalized eigenvalues of the correlation matrix for snapshot solutions of the wind velocity (a) and the retained energy (b) as a function of the reduced basis size. Note that the observed drop for Geometry 2 with $N_{\text{rb}} > 16$ in (b) occurs because $E_n = 1$ for these RB sizes.

PODI

For the reduction by means of PODI, the RB is created through POD, and the mapping between input parameters and POD coefficients is realized via RBF interpolation with a thin-plate spline kernel as shown in Sec. 2.2. Other parameters remain constant compared to the PODG approach as shown in Table 2, except for those related to DEIM, which is not required when applying PODI. The implementation is based on the open-source toolbox *EZyRB* [Demo et al., 2018]. It should be noted that, unlike *RBniCS*, no supremizer stabilization or lifting procedure is implemented in *EZyRB*. However, during the course of the evaluations below, neither instabilities nor issues with boundary conditions could be observed.

Results

In the following, the results of the two approaches are compared using identical test data for both methods. As outlined in Sec. 1, the comparison focuses on the accuracy versus speed-up relation, the amount of data required by both methods, and the ability to extrapolate predictions outside the parameter range considered during training. Looking at the results for approximation accuracy as well as speed-up, Fig. 3 shows that the mean relative L^2 -error rapidly decreases for both methods when increasing the size of the reduced basis. However, for a certain number of reduced basis functions,

Table 2: Parameters of the PODG and PODI ROM, parametrized by the inflow wind velocity. Note that DEIM quantities are not applicable to the PODI approach.

Parameter	Numerical Examples	
	Geometry 1	Geometry 2
Subspace dimension	POD (N_{rb}) DEIM (N_{DEIM})	$N_{\text{rb}} \in [1, 20]$ 20
Snapshots	(POD, DEIM)	50
Test set size	(POD, DEIM)	20

a plateau is reached at a very low error level, where adding more basis functions no longer improves the approximation quality. For the PODG ROM, this plateau aligns closely with the decay of the eigenvalues shown in Fig. 2a. For PODI however, the impact of interpolation is seen by the plateau being reached earlier. Due to its physics-based nature, PODG leads to a significantly lower error compared to PODI. On the other hand, when examining speed-up, it can be seen that PODI consistently provides a high speed-up even with larger reduced basis sizes.

To further investigate how both methods behave for different amount of provided snapshot data, $N_s = \{25, 50, 75, 100\}$ samples of the parameter space are considered. The resulting relative L^2 -error is shown in Fig. 4. It is evident that the ROM constructed with the PODG method approximates the FOM very well even for very few snapshots. In contrast, the prediction accuracy of the ROM constructed with PODI shows to be highly sensitive to the amount of snapshot data when only a few data points are available, but becomes less sensitive as the training data increases. Hence, even with the maximum amount of data, PODI still results in higher errors compared to PODG. Eventually, the ability of the ROMs to extrapolate to parameter values outside the trained range is investigated by splitting the training range so that both ROMs are set up for inflow wind speeds $w_i \in [0.5 \text{ m s}^{-1}, 10.15 \text{ m s}^{-1}]$. Yet, they are still evaluated over the extended parameter range as before, i.e., $w_i \in [0.5 \text{ m s}^{-1}, 20 \text{ m s}^{-1}]$. For a better interpretability of the error, Fig. 5 shows the maximum absolute error over both the parameter range and the computational domain. It can be seen that both ROMs provide small errors for parameters lying inside the parameter range for training. However, outside this range, the errors increase rapidly as the distance between the evaluated parameter and the trained range grows. As also mentioned in Czech et al. [2022], the PODG ROM is slightly better when it comes to extrapolating to values very close to the trained parameter range. This is seen when looking at the maximum absolute error at around $w_i = 11 \text{ m s}^{-1}$. Here, a jump is observed for both methods – for PODG the error increases by about two orders of magnitude, while for PODI, the error jumps by about four orders of magnitude. Despite this, the prediction accuracies of both methods become more similar as the evaluated parameter moves further from the training range. Moreover, it can be observed, that for parameter values far outside the training range, a solution of the reduced system of equations obtained by PODG cannot be always guaranteed.

Discussion

It has been shown that, although PODI offers a greater flexibility and speed-up, the accuracy achieved by this purely data-driven method does not match the accuracy of the physics-based PODG, even when using four times as much training data. Additionally, PODI shows to be highly sensitive to insufficient training data, which causes a rapid decline in prediction accuracy. Regarding the ability to extrapolate to parameter values not included in the training snapshots, both methods perform poorly. Although it can be noted that PODG performs slightly better when extrapolating close to the trained parameter range, a solution of the reduced system cannot be guaranteed further away from it. Eventually, two trade-offs can be identified when choosing between the two methods: First, the higher accuracy achieved by PODG comes at the cost of a lower speed-up – seen by a higher (but acceptable) error at a three times higher speed-up for the PODI ROM. Second, while the non-intrusiveness of PODI offers great flexibility and straightforward implementation, it requires more data and yet results in lower accuracy, as shown in Fig. 4. Nonetheless, since the approximation accuracy of PODI is sufficient for the presented examples and a high speed-up is of great interest for the application, the PODI ROM is extended to handle a system with two parameters — both inflow wind velocity and wind direction.

3.2 Two-parameter case

Building on the results from the previous study, the PODI-based ROM is extended to include a second parameter – the wind direction. Here, a refined version of the mesh shown in Fig. 1b, with approximately 1.7×10^5 degrees of freedom, is used as computational domain. The Dirichlet boundary condition is now defined as $\mathbf{g}_D = w_i [\cos(w_d), \sin(w_d)]^\top$ with the inflow wind velocity w_i in m s^{-1} and the direction w_d in radians [Gioia et al., 2024]. Consequently, the INS problem in Eq. (1) is transformed into an enclosed flow problem, as treated in [Elman et al., 2014, Sec. 9.3.5], without a Neumann boundary condition. As before, the reducibility of the problem is assessed by evaluating the eigenvalues of the correlation matrix and the retained energy for the RB size N_{rb} , as shown in Fig. 6. It can be observed that the decay of the eigenvalues is slower than in the previous case, where only wind intensity has been considered as a parameter. This suggests an increased need for a larger RB. The parameters of the ROM are summarized in Table 3. For the Reynolds number of the two-parameter case, the diameter of the refined mesh around the region of interest, as it can be seen in Fig. 1b, is chosen as the characteristic length for the Reynolds number. The resulting approximation accuracy and the speed-up are presented in Fig. 7. As indicated by the eigenvalues of the correlation matrix, introducing the second parameter makes the problem significantly harder to reduce. Hence, the mean L^2 -error is not as low as in the previous case but remains below 2% for a RB size of twenty. Additionally, a high speed-up of approximately 1000 is achieved by the ROM.

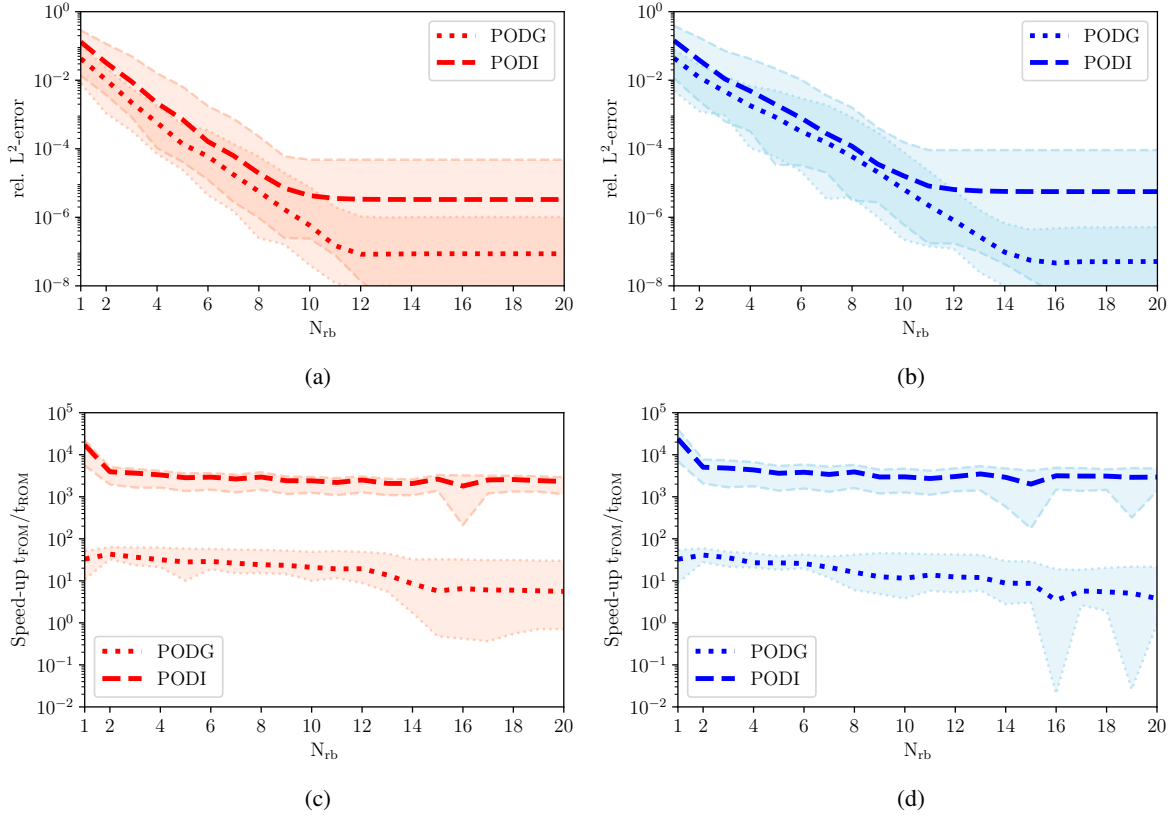


Figure 3: Upper row: relative L^2 -error across the test parameter set for Geometry 1 (a) and Geometry 2 (b). Lower row: speed-up across the test parameter set for Geometry 1 (c) and Geometry 2 (d). The bold line represents the mean value, while the shaded area indicates the range between minimum and maximum L^2 -error and speed-up, respectively.

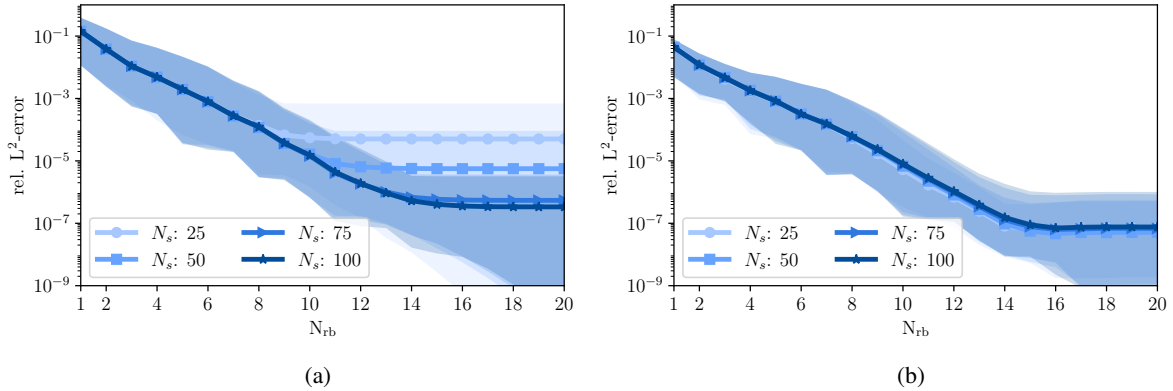


Figure 4: Decay of the minimum, maximum and mean relative L^2 -error across the test parameter set for different sizes of the snapshot set N_s when setting up the ROM by means of PODI (a) and PODG (b). The mean L^2 -errors are indicated by the bold line, while the shaded areas represent the range between minimum and maximum L^2 -error.

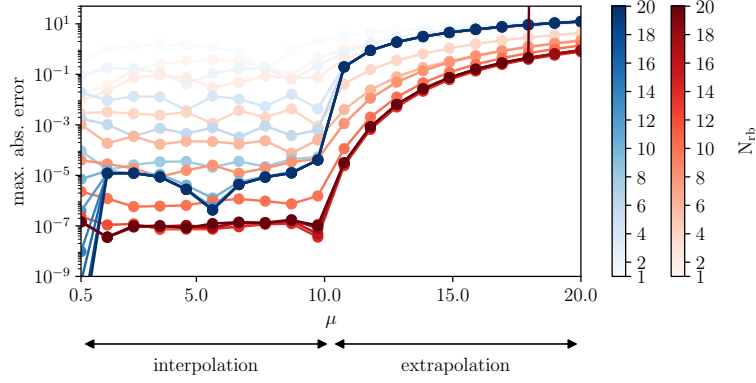


Figure 5: Comparison of interpolation and extrapolation capabilities of both ROMs, based on 50 snapshots for $w_i \in [0.5 \text{ m s}^{-1}, 10.15 \text{ m s}^{-1}]$ and evaluated on 20 testing samples for $w_i \in [0.5 \text{ m s}^{-1}, 20 \text{ m s}^{-1}]$. For good interpretability, the maximum absolute error is shown over the parameter range for different sizes of the RB, with ROMs generated by PODG (red) and PODI (blue). The vertical line at $w_i \approx 18 \text{ m s}^{-1}$ marks a test sample for which no solution was found with PODG.

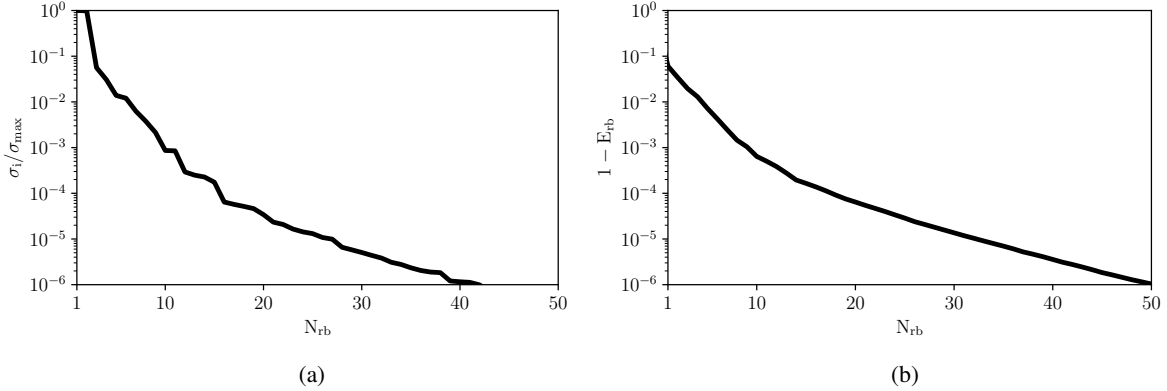


Figure 6: Normalized eigenvalues of the correlation matrix (a) and retained energy (b) by a RB of size N_{rb} for a ROM of the INS problem parametrized by both inflow wind velocity and direction.

Table 3: Parameters of the full-order and reduced-order model featuring a parametric dependence on the inflow wind velocity and direction.

Parameter	Value	
Degrees of freedom	169,462	
Reynolds number	$Re \in [0, 220]$	
Inflow wind velocity (m s^{-1})	$w_i \in [1e - 4, 12]$	
Inflow wind direction (deg)	$w_d \in [0, 360]$	
Subspace POD (N_{rb})	$N_{rb} \in [1, 50]$	
Snapshots	wind intensity w_i	20
	wind direction w_d	150
Test set size	wind intensity w_i	4
	wind direction w_d	30

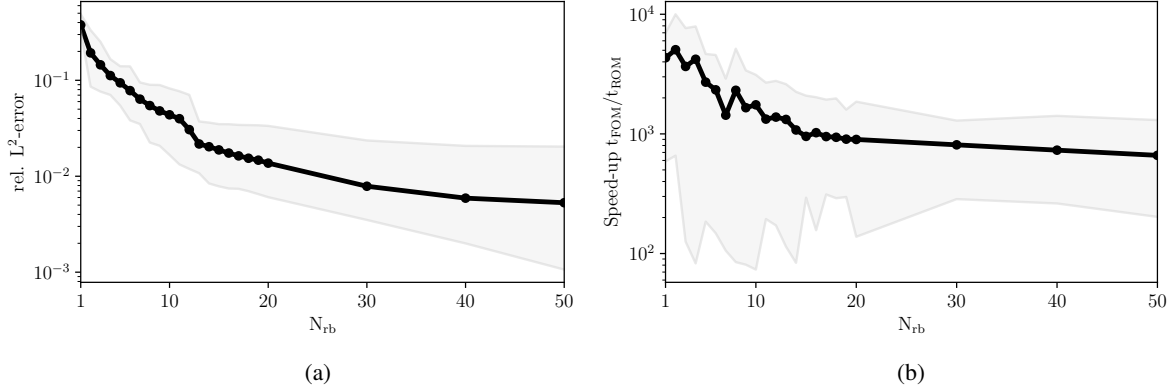


Figure 7: Minimum, maximum and mean L^2 -error (a) and speed-up (b) obtained by the PODI-based ROM developed to account for different inflow wind velocity and direction. The mean error and speed-up are indicated by the bold line, while shaded areas represent the range between minimum and maximum error or speed-up, respectively.

4 Application Case for Crisis Management – Gas Leakage Incident at a Chemical Plant

4.1 Uncertainty quantification for wind measurement errors

The following scenario is based on the application presented in Schneider et al. [2025], where an Emergency Response Inference Mapping (ERIMap) is introduced. The goal is to enable a systematic assessment of emergency situations tailored to support decision-making. To illustrate the approach, a chlorine gas leak at a chemical plant located in Düsseldorf, Germany, is considered. As a model for the dispersion of chlorine gas a Gaussian plume model, as implemented in ALOHA [Jones et al., 2013] is applied. In this work, the modeling approach is extended, by representing the plume’s development through an advection-diffusion problem instead. To facilitate rapid evaluation during emergencies and enable multi-query analysis, the ROM approach presented in Sec. 3.2 is employed to predict the wind field. This way, only the computationally less expensive advection-diffusion problem needs to be solved. To demonstrate the advantages of this approach, the influence of a $\pm 5\%$ uncertainty in wind measurements is explored by using a Monte-Carlo analysis [Fishman, 1996] with 5,000 samples. For this analysis, the mean wind velocity and direction values are derived from one year of wind data collected for Düsseldorf by the German weather service (DWD). The inflow wind velocity and direction are assumed to vary uniformly within a $\pm 5\%$ range around the annual mean, corresponding to an absolute range of $w_i = 4 \pm 0.2 \text{ m s}^{-1}$ for the inflow wind velocity and $w_d = 97 \pm 10 \text{ deg}$ for the wind direction.

To ensure reasonable computational times while maintaining accurate wind field predictions, the ROM for the INS problem, as presented in Sec. 3.2, is applied with $N_{rb} = 20$. Using the resulting wind field predictions, the advection-diffusion problem is solved for $t \in [0 \text{ s}, 100 \text{ s}]$. The resulting distribution of the nodal concentration value at the node with the highest variance after 100 s, shown in Fig. 8, reveals that the concentration values vary widely, ranging from

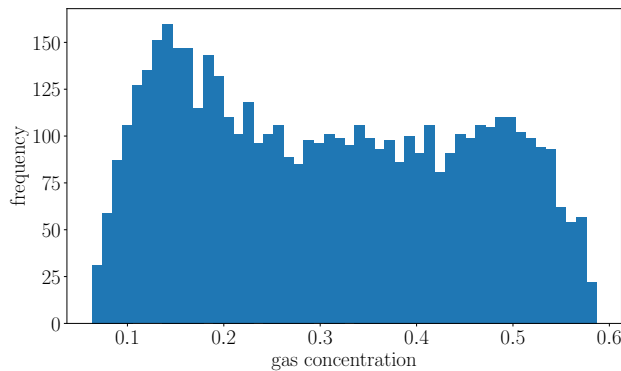


Figure 8: Distribution of gas concentration values $c(\mathbf{x} = \mathbf{x}_{hv}, t = 100 \text{ s})$ stemming from uncertainty in the wind velocity and direction measurements at the location with the highest variance in the domain \mathbf{x}_{hv} at $t = 100 \text{ s}$.

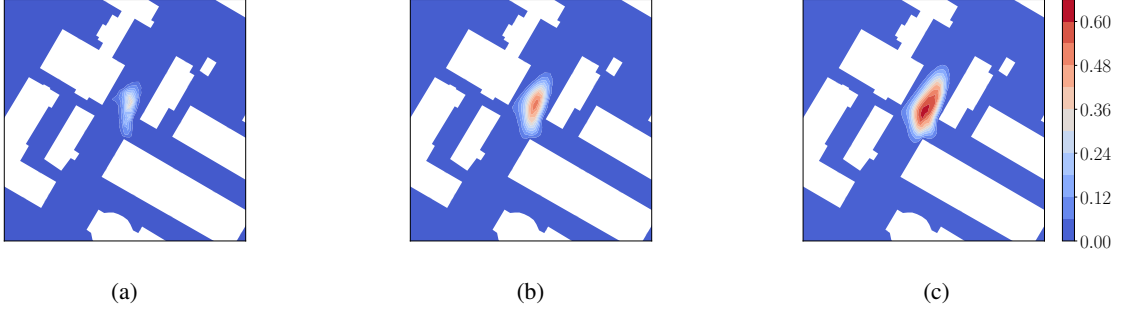


Figure 9: Numerical Monte Carlo results at $t = 100$ s showing areas of minimum (a), expected (b) and maximum (c) gas concentration for varying parameter realizations with concentration values on a scale $[0, 1]$.

nearly no gas concentration and almost 60% gas concentration in the air. Therefore, Fig. 9 focuses on the minimal, expected and maximal concentration fields. The minimum concentration field thereby represents areas where gas presence is guaranteed, while the maximum concentration field highlights regions that could potentially contain gas based on the assumed uncertainties in the input parameters.

4.2 Visualization in interactive dashboard

To enable the practical use of the computed data, the reduced model can be integrated into a digital twin framework and results can be visualized through an interactive dashboard, as shown in Fig. 10. Therein, users can easily adjust the inflow wind direction and velocity directly from the graphical user interface. The ROM then allows for a rapid evaluation of the concentration field based on the user input. Eventually, the concentration field is displayed in such a way that concentration values can be easily accessed by hovering over the specific regions. This can be particularly helpful in emergency situations, for instance, when coordinating evacuation teams, and can also serve as a valuable tool for training exercises. Although the example presented here represents an initial step, the visualization demonstrates how the developed ROM can be effectively used within the context of crisis management. Furthermore, it highlights the benefits of embedding simulations into such frameworks, offering an intuitive interface for real-time decision-making.

5 Conclusion and Outlook

In this paper, a comprehensive comparison between PODI and PODG has been conducted for predicting a parametrized laminar wind field for different inflow wind velocities. The use case is motivated by the scenario of airborne contaminant transport across a built-up area, modeled as a simplified two-dimensional domain with real-world building layouts. The comparison has revealed that both methods provide sufficiently accurate results, though a clear trade-off between approximation accuracy and speed-up has been observed. Furthermore, another trade-off has been identified between the amount of data required to set up the ROM and the accuracy loss that one is willing to accept for the benefits of non-intrusiveness. Given that the accuracy of the ROM generated by PODI has been deemed acceptable, combined with its significant speed-up, the approach has been subsequently extended to account for two parameters – the inflow wind direction and velocity. This extension allows for more realistic modeling. Additionally, potential benefits of a reduced model in the considered scenario, have been demonstrated by performing a Monte Carlo analysis, which can help identifying areas with certain, possible and expected gas concentration based on uncertainties in wind measurements. Eventually, the computed information could be exploited in an easily accessible manner by embedding the ROM-based numerical simulation into an interactive dashboard that visualizes contaminated areas for varying, user-specified wind conditions.

As mentioned, the presented numerical set-up focuses on a two-dimensional representation of a real-world geometry, considering only a two-dimensional flow. Therefore, future work will aim to extend this to three-dimensional flow patterns and higher Reynolds numbers. Additionally, both PODI and PODG rely on linear subspaces, but as Reynolds number increases these linear approaches may no longer yield sufficiently accurate results. Therefore, the application of nonlinear MOR approaches will be a key aspect of future research. Lastly, introducing a reduced model for the AD problem is of high interest to further accelerate the evaluation process.

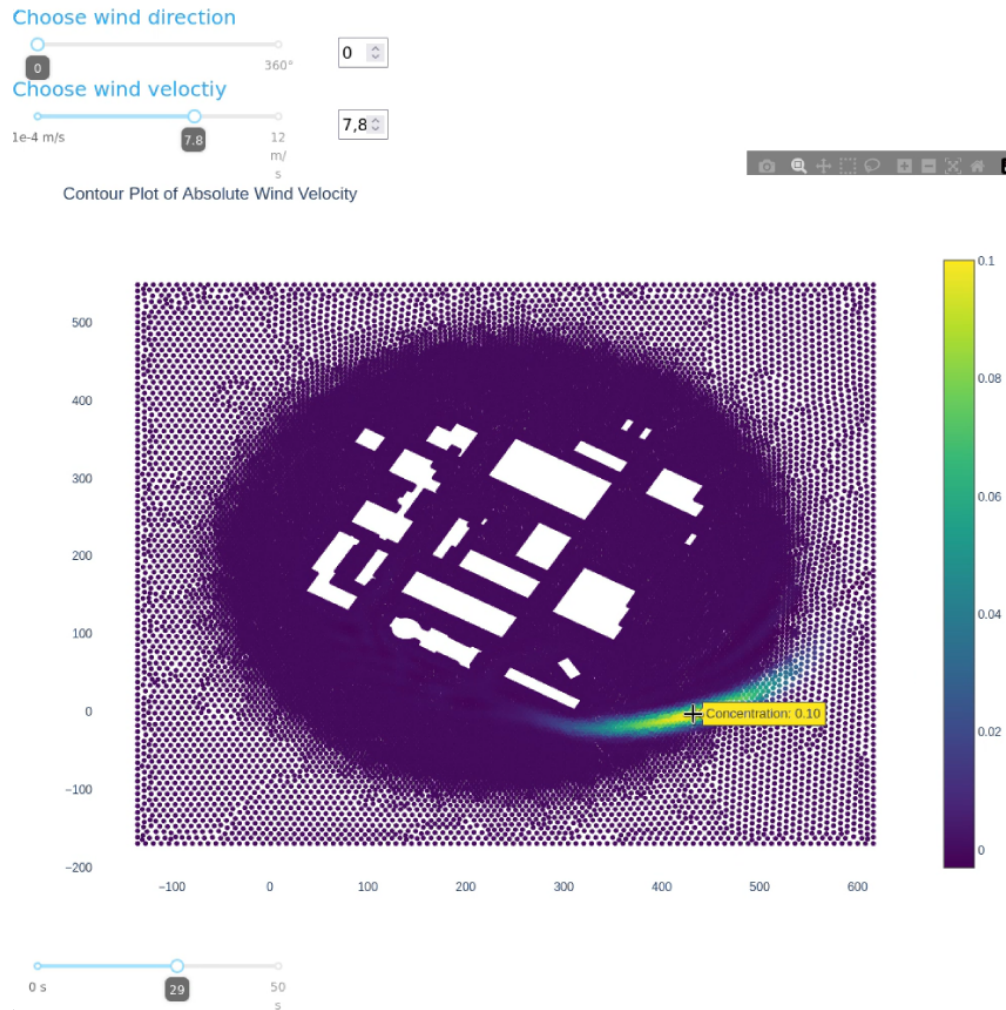


Figure 10: Screenshot of the interactive dashboard displaying fast online evaluations for user-specified parameter values.

Acknowledgment

A.P. acknowledges support by *dtec.bw* - *Digitalization and Technology Research Center of the Bundeswehr* (project *RISK.twin*). *dtec.bw* is funded by the European Union - NextGenerationEU.

Glossary

AD advection diffusion.

CBRN chemical, biological, radiological, nuclear.

CFD computational fluid dynamics.

DEIM discrete empirical interpolation method.

FOM full-order model.

INS incompressible Navier-Stokes.

MOR model order reduction.

POD proper-orthogonal decomposition.

PODG proper-orthogonal decomposition with subsequent Galerkin projection.

PODI proper-orthogonal decomposition with subsequent interpolation.

RB reduced basis.

RBF radial basis function.

ROM reduced-order model.

SUPG streamline upwind Petrov-Galerkin.

SVD singular value decomposition.

References

- S. Owens, S. E. Johnson, and C. J. K. Sandoval. Incident reports: Events reported to the csb under the accidental release reporting rule. Technical report, U.S. Chemical Safety and Hazard Investigation Board, 2025. Volumes 1 – 3. Accessed: 2025-11-17.
- V. Bene, N. Daruka, and B. Elek. A comparative analysis of chemical accident databases and recommendations for improved safety practices. *Honvédségi Szemle*, 152(Special Issue 1-2):136–148, 2024. ISSN 2060-1506. doi:10.35926/HDR.2024.1-2.10.
- M. R. Gomez, S. Casper, and E. A. Smith. The csb incident screening database: description, summary statistics and uses. *Journal of hazardous materials*, 159(1):119–129, 2008. ISSN 0304-3894. doi:10.1016/j.jhazmat.2007.07.122.
- Coming Clean Inc. Key findings 2021–2023: Chemical disaster prevention, 2023. Accessed: 2025-11-12.
- D. J. Carruthers, R. J. Holroyd, J.C.R. Hunt, W. S. Weng, A. G. Robins, D. D. Apsley, D. J. Thompson, and F. B. Smith. Uk-adms: A new approach to modelling dispersion in the earth’s atmospheric boundary layer. *Journal of Wind Engineering and Industrial Aerodynamics*, 52:139–153, 1994. ISSN 01676105. doi:10.1016/0167-6105(94)90044-2.
- R. Jones, W. Lehr, D. Simecek-Beatty, and R. M. Reynolds. Aloha® (areal locations of hazardous atmospheres) 5.4.4: Technical documentation. Technical Report NOS OR&R 43, U.S. Department of Commerce, NOAA Technical Memorandum, Seattle, WA, 2013. URL <https://repository.library.noaa.gov/view/noaa/2669>. Emergency Response Division, NOAA.
- A. J. Cimorelli, S. G. Perry, A. Venkatram, J. C. Weil, R. J. Paine, R. B. Wilson, R. F. Lee, W. D. Peters, and R. W. Brode. Aermod: A dispersion model for industrial source applications. part i: General model formulation and boundary layer characterization. *Journal of Applied Meteorology*, 44(5):682–693, 2005. ISSN 0894-8763. doi:10.1175/JAM2227.1.
- N.Kh. Arystanbekova. Application of gaussian plume models for air pollution simulation at instantaneous emissions. *Mathematics and Computers in Simulation*, 67(4-5):451–458, 2004. doi:10.1016/j.matcom.2004.06.023.
- E. Holzbecher. 2d and 3d transport solutions (gaussian puffs and plumes). In *Environmental modeling*, pages 303–316. Springer, 2011. doi:10.1007/978-3-642-22042-5_16.
- H. Snoun, M. Krichen, and H. Chérif. A comprehensive review of gaussian atmospheric dispersion models: current usage and future perspectives. *Euro-Mediterranean Journal for Environmental Integration*, 8(1):219–242, 2023. ISSN 2365-6433. doi:10.1007/s41207-023-00354-6.
- M. Schneider, L. Halekotte, T. Comes, D. Lichte, and F. Fiedrich. Emergency response inference mapping (erimap): A bayesian network-based method for dynamic observation processing. *Reliability Engineering & System Safety*, 255: 110640, 2025. ISSN 09518320. doi:10.1016/j.ress.2024.110640.
- J. Boris. The threat of chemical and biological terrorism: preparing a response. *Computing in Science & Engineering*, 4(2):22–32, 2002. ISSN 15219615. doi:10.1109/5992.988644.
- G. Patnaik, J. P. Boris, F. F. Grinstein, J. P. Iselin, and D. Hertwig. Large scale urban simulations with fct. In D. Kuzmin, R. Löhner, and S. Turek, editors, *Flux-Corrected Transport*, Scientific Computation, pages 91–117. Springer Netherlands, Dordrecht, 2012. ISBN 978-94-007-4037-2. doi:10.1007/978-94-007-4038-9_4.

- J. Kukkonen, T. Olsson, D. M. Schultz, A. Baklanov, T. Klein, A. I. Miranda, A. Monteiro, M. Hirtl, V. Tarvainen, M. Boy, et al. A review of operational, regional-scale, chemical weather forecasting models in europe. *Atmospheric Chemistry and Physics*, 12(1):1–87, 2012. doi:10.5194/acp-12-1-2012.
- M. Khamlich, G. Stabile, G. Rozza, L. Környei, and Z. Horváth. A physics-based reduced order model for urban air pollution prediction. *Computer Methods in Applied Mechanics and Engineering*, 417:116416, 2023. doi:10.1016/j.cma.2023.116416.
- M. von Danwitz, J. Bonari, P. Franz, and L. Kühn. Contaminant dispersion simulation in a digital twin framework for critical infrastructure protection. In *9th European Congress on Computational Methods in Applied Sciences and Engineering*. CIMNE, 2024. doi:10.23967/eccomas.2024.301.
- S. Ulfah, S. A. Awalludin, and Wahidin. Advection-diffusion model for the simulation of air pollution distribution from a point source emission. *Journal of Physics: Conference Series*, 948:012067, 2018. doi:10.1088/1742-6596/948/1/012067.
- G. Rozza, G. Stabile, and F. Ballarin. *Advanced Reduced Order Methods and Applications in Computational Fluid Dynamics*. Society for Industrial and Applied Mathematics, Philadelphia, PA, 2022. ISBN 978-1-61197-724-0. doi:10.1137/1.9781611977257.
- A. Quarteroni, A. Manzoni, and F. Negri. *Reduced basis methods for partial differential equations: An introduction*, volume 92 of *UNTEXT La Matematica per il 3+2*. Springer, Cham, 2015. ISBN 978-3-319-15431-2. doi:10.1007/978-3-319-15431-2.
- P. Benner, S. Grivet-Talocia, A. Quarteroni, G. Rozza, W. Schilders, and L. M. Silveira, editors. *Model Order Reduction: Volume 1: System- and data-driven methods and algorithms*, volume 1 of *Model order reduction*. De Gruyter, Berlin and Boston, 2021. ISBN 978-3-11-049896-7. doi:10.1515/9783110498967.
- P. Benner, W. Schilders, S. Grivet-Talocia, A. Quarteroni, G. Rozza, and L. Miguel Silveira, editors. *Model Order Reduction: Volume 2: Snapshot-Based Methods and Algorithms*, volume 2 of *Model order reduction*. De Gruyter, Berlin/Boston, 2020. ISBN 978-3-11-067149-0. doi:10.1515/9783110671490.
- F. Pichi, M. Strazzullo, F. Ballarin, and G. Rozza. Chapter 2: Finite element-based reduced basis method in computational fluid dynamics. In G. Rozza, G. Stabile, and F. Ballarin, editors, *Advanced Reduced Order Methods and Applications in Computational Fluid Dynamics*, pages 13–58. Society for Industrial and Applied Mathematics, Philadelphia, PA, 2022. ISBN 978-1-61197-724-0. doi:10.1137/1.9781611977257.ch2.
- A. Quarteroni. *Reduced Order Methods for Modeling and Computational Reduction*, volume 9 of *MS&A*. Springer International Publishing AG, Cham, 1st ed. edition, 2014. ISBN 978-3-319-02090-7. doi:10.1007/978-3-319-02090-7.
- J. S. Hesthaven, G. Rozza, and B. Stamm. *Certified Reduced Basis Methods for Parametrized Partial Differential Equations*. Springer International Publishing, Cham, 2016. ISBN 978-3-319-22469-5. doi:10.1007/978-3-319-22470-1.
- M. Tezzele, N. Demo, G. Stabile, and G. Rozza. Chapter 9: Nonintrusive data-driven reduced order models in computational fluid dynamics. In G. Rozza, G. Stabile, and F. Ballarin, editors, *Advanced Reduced Order Methods and Applications in Computational Fluid Dynamics*, pages 203–222. Society for Industrial and Applied Mathematics, Philadelphia, PA, 2022. ISBN 978-1-61197-724-0. doi:10.1137/1.9781611977257.ch9.
- J. Yu, C. Yan, and M. Guo. Non-intrusive reduced-order modeling for fluid problems: A brief review. *Proceedings of the Institution of Mechanical Engineers, Part G: Journal of Aerospace Engineering*, 233(16):5896–5912, 2019. doi:10.1177/0954410019890721.
- C. Czech, M. Lesjak, C. Bach, and F. Duddeck. Data-driven models for crashworthiness optimisation: intrusive and non-intrusive model order reduction techniques. *Structural and Multidisciplinary Optimization*, 65(7), 2022. doi:10.1007/s00158-022-03282-1.
- P. Conti, M. Guo, A. Manzoni, A. Frangi, S. L. Brunton, and J. N. Kutz. Multi-fidelity reduced-order surrogate modelling. *Proceedings of the Royal Society A: Mathematical, Physical and Engineering Sciences*, 480(2283), 2024. ISSN 1364-5021. doi:10.1098/rspa.2023.0655.
- F. Ballarin, A. Manzoni, A. Quarteroni, and G. Rozza. Supremizer stabilization of pod–galerkin approximation of parametrized steady incompressible navier–stokes equations. *International Journal for Numerical Methods in Engineering*, 102(5):1136–1161, 2015a. doi:10.1002/nme.4772.
- R. Vinuesa and S. L. Brunton. Enhancing computational fluid dynamics with machine learning. *Nature computational science*, 2(6):358–366, 2022. doi:10.1038/s43588-022-00264-7.

- F. Regazzoni, S. Pagani, M. Salvador, L. Dede', and A. Quarteroni. Learning the intrinsic dynamics of spatio-temporal processes through latent dynamics networks. *Nature communications*, 15(1):1834, 2024. doi:10.1038/s41467-024-45323-x.
- G. Veiga-Piñeiro, P. Dominguez, E. Aldao, G. Fontenla-Carrera, F. Veiga-López, E. B. Martín, and H. González-Jorge. Physics-aware wind surrogate model for uav aerodynamic response assessment. *International Journal of Numerical Methods for Heat & Fluid Flow*, 2025. doi:10.1108/HFF-11-2024-0857.
- S. Masoumi-Verki, F. Haghghat, and U. Eicker. A review of advances towards efficient reduced-order models (rom) for predicting urban airflow and pollutant dispersion. *Building and Environment*, 216:108966, 2022. ISSN 03601323. doi:10.1016/j.buildenv.2022.108966.
- R. Arcucci, D. Xiao, F. Fang, I. M. Navon, P. Wu, C. C. Pain, and Y. Guo. A reduced order with data assimilation model: Theory and practice. *Computers & Fluids*, 257:105862, 2023. ISSN 00457930. doi:10.1016/j.compfluid.2023.105862.
- C. Reisch, A. Navas-Montilla, and I. Özgen-Xian. Analytical and numerical insights into wildfire dynamics: Exploring the advection–diffusion–reaction model. *Computers & Mathematics with Applications*, 158:179–198, 2024. ISSN 08981221. doi:10.1016/j.camwa.2024.01.024.
- C. Zhong, S. Cheng, M. Kasoar, and R. Arcucci. Reduced-order digital twin and latent data assimilation for global wildfire prediction. *Natural Hazards and Earth System Sciences*, 23(5):1755–1768, 2023. doi:10.5194/nhess-23-1755-2023.
- M. R. Schuster, N. Dirkes, F. Key, S. Elgeti, and M. Behr. Exploring the influence of parametrized pulsatility on left ventricular washout under lvad support: a computational study using reduced-order models. *Computer Methods in Biomechanics and Biomedical Engineering*, 28(6):800–817, 2025. doi:10.1080/10255842.2024.2320747.
- F. Chinesta, D. Baillargeat, and B. Genest. Descartes: Hybrid artificial intelligence for optimal planning and decision making in urban systems. In *AI4X 2025 International Conference*, 2025. URL <https://openreview.net/pdf?id=GcV38AcUbu>.
- T. Ritter, J. Euler, S. Ulbrich, and O. von Stryk. Decentralized dynamic data-driven monitoring of atmospheric dispersion processes. *Procedia Computer Science*, 80:919–930, 2016. ISSN 18770509. doi:10.1016/j.procs.2016.05.382.
- M. Mattuschka, N. an der Lan, M. von Danwitz, D. Wolff, and A. Popp. Goal-oriented optimal sensor placement for pde-constrained inverse problems in crisis management, 2025.
- G. Padula, M. Girfoglio, and G. Rozza. A brief review of reduced order models using intrusive and non-intrusive techniques. *PAMM*, 24(4), 2024. ISSN 1617-7061. doi:10.1002/pamm.202400210.
- B. Karasözen, S. Yıldız, and M. Uzunca. Intrusive and data-driven reduced order modelling of the rotating thermal shallow water equation. *Applied Mathematics and Computation*, 421:126924, 2022. ISSN 00963003. doi:10.1016/j.amc.2022.126924.
- J. Bonari, L. Kühn, M. von Danwitz, and A. Popp. Towards real-time urban physics simulations with digital twins. In *2024 28th International Symposium on Distributed Simulation and Real Time Applications (DS-RT)*, pages 18–25. IEEE, 2024. doi:10.1109/DS-RT62209.2024.00013.
- H. C. Elman, D. J. Silvester, and A. J. Wathen. *Finite elements and fast iterative solvers: with applications in incompressible fluid dynamics*. Numerical mathematics and scientific computation. Oxford University Press, Oxford, second edition, 2014. ISBN 9780199678808.
- M. S. Alnaes, J. Blechta, J. Hake, A. Johansson, B. Kehlet, A. Logg, C. N. Richardson, J. Ring, M. E. Rognes, and G. N. Wells. The fenics project version 1.5. *Archive of Numerical Software*, 3, 2015. doi:10.11588/ans.2015.100.20553.
- A. N. Brooks and T. J. R. Hughes. Streamline upwind/petrov-galerkin formulations for convection dominated flows with particular emphasis on the incompressible navier-stokes equations. *Computer Methods in Applied Mechanics and Engineering*, 32(1-3):199–259, 1982. doi:10.1016/0045-7825(82)90071-8.
- M. Behr. Simplex space–time meshes in finite element simulations. *International Journal for Numerical Methods in Fluids*, 57(9):1421–1434, 2008. doi:10.1002/fld.1796.
- M. von Danwitz, I. Voulis, N. Hosters, and M. Behr. Time–continuous and time–discontinuous space–time finite elements for advection–diffusion problems. *International Journal for Numerical Methods in Engineering*, 124(14): 3117–3144, 2023. doi:10.1002/nme.7241.
- K. Key, M. R. A. Abdelmalik, S. Elgeti, T. J. R. Hughes, and F. A. Baidoo. Finite element and isogeometric stabilized methods for the advection-diffusion-reaction equation. *Computer Methods in Applied Mechanics and Engineering*, 417:116354, 2023. doi:10.1016/j.cma.2023.116354.

- S. Hijazi, M. Freitag, and N. Landwehr. Pod-galerkin reduced order models and physics-informed neural networks for solving inverse problems for the navier–stokes equations. *Advanced Modeling and Simulation in Engineering Sciences*, 10(1), 2023. doi:10.1186/s40323-023-00242-2.
- S. Lorenzi, A. Cammi, L. Luzzi, and G. Rozza. Pod-galerkin method for finite volume approximation of navier–stokes and rans equations. *Computer Methods in Applied Mechanics and Engineering*, 311:151–179, 2016. ISSN 00457825. doi:10.1016/j.cma.2016.08.006.
- S. Chaturantabut and D. C. Sorensen. Nonlinear model reduction via discrete empirical interpolation. *SIAM Journal on Scientific Computing*, 32(5):2737–2764, 2010. ISSN 1064-8275. doi:10.1137/090766498.
- G. Rozza, F. Ballarin, L. Scandurra, and F. Pichi. *Real Time Reduced Order Computational Mechanics*, volume 5. Springer, Cham, 2024. ISBN 978-3-031-49891-6. doi:10.1007/978-3-031-49892-3.
- T. Bui-Thanh, M. Damodaran, and K. Willcox. Proper orthogonal decomposition extensions for parametric applications in compressible aerodynamics. In *21st AIAA Applied Aerodynamics Conference*, Reston, Virginia, 2003. American Institute of Aeronautics and Astronautics. ISBN 978-1-62410-092-5. doi:10.2514/6.2003-4213.
- A. Bērziņš, J. Helmig, F. Key, and S. Elgeti. Standardized non-intrusive reduced order modeling using different regression models with application to complex flow problems, 2020.
- D. Xiao, F. Fang, C. Pain, and G. Hu. Non-intrusive reduced-order modelling of the navier–stokes equations based on rbf interpolation. *International Journal for Numerical Methods in Fluids*, 79(11):580–595, 2015. ISSN 0271-2091. doi:10.1002/flid.4066.
- F. Ballarin, A. Sartori, and G. Rozza. Rbnics – reduced order modelling in fenics, 2015b. URL <https://www.rbnicsproject.org/>.
- N. Demo, M. Tezzele, and G. Rozza. Ezyrb: Easy reduced basis method. *Journal of Open Source Software*, 3(24):661, 2018. doi:10.21105/joss.00661.
- D. Giovanni Gioia, J. Bonari, D. Lichte, and A. Popp. Sequential drone routing for data assimilation on a 2d airborne contaminant dispersion problem. In *2024 Sensor Data Fusion: Trends, Solutions, Applications (SDF)*, pages 1–8. IEEE, 2024. ISBN 979-8-3315-2744-0. doi:10.1109/SDF63218.2024.10773899.
- G. S. Fishman. *Monte Carlo*. Springer New York, New York, NY, 1996. ISBN 978-1-4419-2847-4. doi:10.1007/978-1-4757-2553-7.